KeAi
CHINESE ROOTS
GLOBAL IMPACT

Available online at www.sciencedirect.com

ScienceDirect

Green Energy & Environment 5 (2020) 506–512

www.keaipublishing.com/gee

Research paper

Realizing optimal hydrogen evolution reaction properties via tuning phosphorous and transition metal interactions

Haishun Jiang [a], Siyu Zhao [b], Wenyao Li [a,b,*], Tobias P. Neville [b], Isil Akpinar [b,d], Paul R. Shearing [b], Dan J.L. Brett [b,*], Guanjie He [b,c,*]

[a] School of Materials Engineering, Shanghai University of Engineering Science, Shanghai, 201620, China
[b] Electrochemical Innovation Lab, Department of Chemical Engineering, University College London, London, WC1E 7JE, United Kingdom
[c] School of Chemistry, University of Lincoln, Joseph Banks Laboratories, Green Lane, Lincoln, LN6 7DL, United Kingdom
[d] Faculty of Engineering, Environmental Engineering, Aksaray University, Aksaray, 68100, Turkey

Received 22 June 2020; revised 12 July 2020; accepted 13 July 2020
Available online 16 July 2020

Abstract

Hydrogen is one of the most attractive renewables for future energy application, therefore it is vital to develop cost-effective and highly-efficient electrocatalysts for the hydrogen evolution reaction (HER) to promote the generation of hydrogen from mild methods. In this work, Co–Mo phosphide nanosheets with the adjustable ratio of Co and Mo were fabricated on carbon cloth by a facile hydrothermal-annealing method. Owing to the unique nanostructures, abundant active surfaces and small resistance were achieved. Excellent electrocatalytic performances are obtained, such as the small overpotential of ~67.3 mV to realize a current density of 10 mA cm^{-2} and a Tafel slope of 69.9 mV dec^{-1}. Rapid recovery of the current response under multistep chronoamperometry is realized and excellent stability retained after the CV test for 2000 cycles. The change of electronic states of different elements was carefully studied which suggested the optimal electrochemical performance can be realized by tuning phosphorous and metal interactions.

Keywords: Co-Mo Phosphide; Nanosheets; Hydrogen evolution reaction; Metal-phosphorous interactions

1. Introduction

Using renewable sources of electricity, electrolysis of water is a clean source of 'green' hydrogen that can be delivered at large-scale in an environmental-friendly process and with very high purity [1]. The overall water electrolytic devices consist of the hydrogen evolution reaction (HER) on the cathode and oxygen evolution reaction (OER) on the anode [2,3]. Over the past decade, plentiful efforts have been paid to invent the high-performance, reliable, and low-cost electrocatalysts for both HER and OER. Compared with expensive Pt-based commercial electrocatalysts, transition metals such as Ni [4], Co [5,6], Mo [7], and Fe [8] in compounds consist of oxides [9], hydroxides [10], nitrides [11], sulphides [12], and phosphides [13] have been extensively studied due to their abundance and potentially tunable electrocatalytic properties [14].

Recently, Co and Mo based materials have been comprehensively researched for HER electrocatalysts. For example, Jing et al. [15] developed a Zn-incorporated cobalt phosphide formed on the Ni foam catalyst which exhibits an excellent HER performance (the overpotential of 172 mV at 100 mA cm^{-2}) in 1 M KOH electrolyte; the results indicating a Volmer-Heyrovsky mechanism for the catalytic process. Xiao et al. [16] demonstrated an approach involving carbon wrapped Co/Ni-doped MoP nanoparticles for the HER. The

* Corresponding authors. School of Materials Engineering, Shanghai University of Engineering Science, Shanghai, 201620, China.
E-mail addresses: liwenyao314@gmail.com (W. Li), d.brett@ucl.ac.uk (D.J.L. Brett), g.he@ucl.ac.uk (G. He).

https://doi.org/10.1016/j.gee.2020.07.009

optimized electrode achieves a small overpotential of 102 mV at 10 mA cm^{-2}. The experimental plus DFT results indicate the hydrogen adsorption energy was optimized by Co/Ni doping and a major enhancement of HER performance was achieved. Nevertheless, much of the single transition metal-based electrocatalysts suffer the constraints due to their intrinsic activities, and the way of tuning single chemical compositions to adjust and balance the adsorption and desorption energy barriers of the intermediates is difficult. However, by conjoining two transition metals or more, electrocatalyst characteristics can be tuned to achieve improved HER performance [17]. For example, Fang et al. [18] fabricated NiCoP nanosheet electrocatalysts for HER, which showed a tiny overpotential of 58 mV at the current density of 10 mA cm^{-2} in 1M KOH electrolyte and long-term durability ascribed to the outstanding electronic conductivity, the synergistic effect from the bimetal atoms and the overall structural stability of the catalysts. Bandal et al. [19] developed an FeCoO−NF electrocatalyst which exhibited a relatively small overpotential of 100 mV to achieve 10 mA cm^{-2} in the alkaline electrolyte. The optimized catalyst is better than its CoO counterpart. However, optimizing the ratio of different transition metals to adjust the electronic structure and hydrogen evolution properties is rarely studied.

Metal phosphides have been revealed as a type of competent HER catalysts owing to their high electronic conductivity and the enhanced adsorption energy of H* from P^{3-}. For example, Jiang et al. [20] reported a CoP_3/CoMoP nanosheet grown on nickel foam. The resulting catalyst exhibits a small overpotential of 110 mV at the current density of 10 mA cm^{-2} and good durability in 1 M KOH, the properties are significantly better than that of $CoMoO_4$ (251 mV), which proves the phosphatization process could improve the electric conduction and enhance the HER performance. Dai et al. [21] synthesized a pyrrhotite-type cobalt monophosphosulfide material for HER which demonstrates a low overpotential of 141 mV at 10 mA cm^{-2} in an alkaline electrolyte. By adjusting the phosphating and vulcanization degree, the P/S atomic ratio of cobalt sulfide monophosphate could be adjusted to activate Co^{3+}/Co^{2+}, which shows that its electrocatalytic activity is significantly improved. Moreover, recently, it was proved that both $P–O^{1-}$ and Co^{3+}-OH^- are promising surface active sites in P-doped β-$CoMoO_4$ for the HER [22], but tuning the metal species/amounts and phosphorous interactions are less considered to realize the best performance.

In this work, the synthesis of Co−Mo phosphide nanosheets is reported using a simple hydrothermal-annealing method. Co−Mo oxides could be obtained by hydrothermal reaction of carbon cloth and metal precursors, then PH_3 produced by the decomposition of NaH_2PO_2 at a high temperature will react directly with Co−Mo oxides nanosheet to generate Co−Mo phosphides. Owing to the unique structures that endow rich active sites, an overpotential of only 67.3 mV is required to deliver a current density at 10 mA cm^{-2} and a small Tafel slope of only 69.9 mV dec^{-1} in the electrolyte of 1 M KOH.

2. Experimental section

2.1. Synthetic procedures

2.1.1. Carbon cloth pre-treatment

Firstly, the carbon cloth (CC, from Toray Company of Japan) was cut into 2 × 3 cm^2 and soaked in 30 mL of 3M nitric acid for 8 h. Then, it was immersed with acetone and exposed to an ultrasonic treatment for 30 min. After that, the CC was washed continuously with deionized (DI) water until the pH became neutral. Finally, the wet CC was dried at 60 °C in the oven.

2.1.2. Synthesis of different proportions of Co−Mo oxides

Co−Mo oxides with different proportions were synthesized directly using a single-step hydrothermal process [23]. Briefly, $Co(CH_3COO)_2 \cdot 4H_2O$ and $NaMoO_4 \cdot 2H_2O$ with different ratios (molar ratios of 0.33:0.66; 0.5:0.5; 0.25:0.75) were transferred to a beaker. Then, 35 mL of DI water was added and then stirred for 10 min until completely mixed. The mixed solution was then poured to a 50 mL PTFE liner. A treated CC was put into the solution and sealed for reaction. The hydrothermal reaction was set at 160 °C for 6 h. After cooling down to the room temperature, the CC was washed with DI water several times and dried at 60 °C in the oven.

2.1.3. Synthesis of Co−Mo phosphide nanosheets

NaH_2PO_2 (molar ratio of cobalt−molybdenum complex and NaH_2PO_2 is 1:10) was used as the phosphorus source. A schematic figure of the synthesis of different Co−Mo phosphide electrodes is shown in Fig. 1. NaH_2PO_2 and Co−Mo oxides/CC were put at both ends of the crucible and the crucible was installed at the inlet of the tube furnace. The heating rate was 3 °C min^{-1}. When the furnace temperature reached 350 °C, the boat was pushed into the heating zone and kept at 350 °C for 2 h. The whole annealing process was performed under a nitrogen atmosphere. Finally, the Co−Mo phosphide/CC was cooled naturally down to room temperature and collected.

2.2. Characterization

The obtained materials were characterized by X-ray diffractometer (XRD, Rigaku, Co-Ka radiation) for phase identification, scanning electron microscope (SEM, Hitchi, S-4800), and transmission electron microscope (TEM, JEOL, JEM-2100F) equipped with EDS for morphology evaluation. The characteristic peaks of X-ray photoelectron spectra (XPS) were collected from a PHI Quantum-2000 electron spectrometer (Ulvac-Phi, Japan). The software used to measure the thickness of nanosheets was Nano Measurer 1.2.5.

2.3. Electrochemical measurements

The three-electrode system was used and measured with an Autolab electrochemical workstation (PGSTAT 302N,

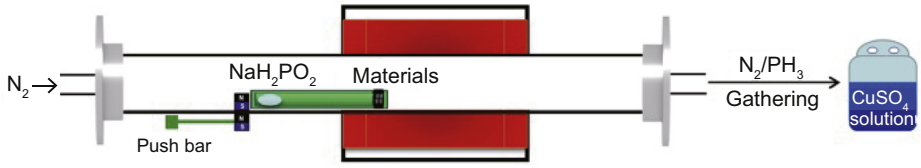

Fig. 1. The process of phosphating cobalt-molybdenum oxides of different proportions after obtaining from the hydrothermal treatment.

Metrohm China Ltd.) in 1.0 M KOH (pH = 13.6) solution. The final obtained products were cut into 1 × 0.5 cm^2 and used as working electrodes directly. The commercial Pt/C electrode was fabricated by using 20% Pt/C (3 mg) homogeneous ink ($V_{Nafion}/V_{ethanol}/V_{water}$ = 10 μL/60 μL/230 μL), the areal loading weight of the materials was 2.2 mg cm^{-2}. The analyses for HER were conducted at a scan rate of 2 mV s^{-1} by linear sweep voltammetry (LSV) test with the iR compensation (90%) after the activation of cyclic voltammetry (CV) at the scan rate of 10 mV s^{-1}. All potentials in this work were converted to the reversible hydrogen electrode (RHE) for easy comparison. The conversion between standard electrodes was performed using the equation: $E_{vs.\ RHE} = E_{vs.\ Ag/AgCl} + 0.059 \times pH + 0.197$ V. The electrochemical impedance spectroscopy (EIS) measurements were carried out by using the FRA impedance potentiostatic mode, the results were obtained biased with an AC voltage at 2 mV over the frequency range from 0.1 to 10^5 Hz. To evaluate the electrochemical surface area, the CV tests with the potential range from 0.197–0.297 V *vs.* RHE were tested. The sweep rates ranged from 2 to 10 mV s^{-1}.

3. Results and discussion

The crystal structure of the Co–Mo oxide and Co–Mo phosphide samples were first characterized by XRD. As displayed in Fig. 2a, the XRD pattern for the $Co_{0.33}Mo_{0.66}O$ is accorded with the $CoMoO_4$ (JCPDS No. 02-0868). The XRD patterns of Co–Mo phosphide materials with different ratios of Co and Mo are closely consistent with the CoMoP (JCPDS No. 71-0478), the peaks are marked with γ. With the Co:Mo of 0.25:0.75, there is a new crystal phase which is speculated to be MoP (JCPDS No. 24-0771). The low-magnification SEM image of $Co_{0.33}Mo_{0.66}P$ composites is shown in Fig. 2b, it can be seen that the $Co_{0.33}Mo_{0.66}P$ materials are homogeneously grown on the carbon fibers, the inset is a SEM image of carbon fibers with lower magnification, which shows that there are nearly no defects generated after growing $Co_{0.33}Mo_{0.66}P$ composites. Fig. 2c is an enlarged SEM image of the carbon fiber, which shows the nanosheet morphology of $Co_{0.33}Mo_{0.66}P$ and that they grow on the carbon fibers densely and homogeneously. Fig. 2d further that demonstrates the nanosheets are cross-linked with the thickness ranging from 10 to 28 nm, and the average thickness is ~20 nm. In addition, the products with different ratios of Co and Mo, i.e., $Co_{0.5}Mo_{0.5}P$ and $Co_{0.25}Mo_{0.75}P$, are also characterized by SEM and shown in Fig. S1. All of the materials show sheet-like morphologies but with different thicknesses. The thickness of $Co_{0.5}Mo_{0.5}P$ nanosheets ranges from 18 to 45 nm and the average thickness is ~30 nm, while there are many defects on the carbon fibres (Fig. S1a); the thickness of $Co_{0.25}Mo_{0.75}P$ nanosheets range from 8 to 23 nm, the average thickness reduces to 15 nm. However, from the SEM image in Fig. S1d, the nanosheets agglomerate to form disorderly clusters; this causes a very dense surface, which is difficult to uniformly cover the carbon fibres, thus this significantly influences the HER properties. Fig. 2e and Figs. S2, S3 are the EDS spectra of Co–Mo phosphide samples, indicating the P element is successfully doped into Co–Mo structures.

The $Co_{0.33}Mo_{0.66}P$ sample was further characterized by TEM, it was found that the nanosheets are stacked together in Fig. 3a, Fig. 3b shows a thin edge part of one nanosheet, the inset shows two HRTEM images obtained from the white rectangle part, which displays well-defined lattice fringes, and the measured interplanar distances, i.e., 0.21, 0.28 and 0.32 nm could be assigned to the typical (211), (111) and (011) planes of cobalt molybdenum phosphides, respectively. Besides, the elemental mapping images (Fig. 3c–f) of $Co_{0.33}Mo_{0.66}P$ nanosheets exhibit the Co, Mo and P elements are homogeneously dispersed on the nanosheets, which proves the formation of Co–Mo phosphide composites.

The XPS characterization is adopted to detect the elemental composition of the materials. The high-resolution XPS spectra of Co 2p, Mo 3d and P 2p for the $Co_{0.25}Mo_{0.75}P$, $Co_{0.33}Mo_{0.66}P$ and $Co_{0.50}Mo_{0.50}P$ are displayed in Fig. 4 (XPS survey spectra are in Fig. S4). According to Fig. 4a, the two strong peaks at binding energy (BE) of 782.2 and 798.3 eV could be indexed to Co^{2+} species. Two small peaks at 786.5 and 803.1 eV were ascribed to satellite peaks of Co. Two peaks at 779.2 and 794.1 eV could be assigned to Co^{3+} species [22,24]. By comparing the content of Co^{2+} and Co^{3+} species, the Co^{3+} species of $Co_{0.33}Mo_{0.66}P$ (30.5%) is higher than that of the $Co_{0.25}Mo_{0.75}P$ (19.5%) and $Co_{0.50}Mo_{0.50}P$ (21.9%). In Fig. 4b, the binding energies at 232.3 and 236.1 eV are corresponded with Mo^{6+} $3d_{5/2}$ and $3d_{3/2}$, respectively. Two peaks at 233.9 eV and 230.6 eV are ascribed to Mo^{4+} species. Another two peaks at 228.3 and 233.3 eV could be assigned to $Mo^{\delta+}$ ($0 < \delta < 4$) oxides [7,25]. The Mo^{4+} and $Mo^{\delta+}$ species could be derived from the reduction process when the pristine material was annealed with P source in the tube furnace. As displayed in Fig. 4c, the binding energies locate at 129.9 and 131.0 eV could be indexed to P^{3-} species in the P 2p spectrum. The BE of

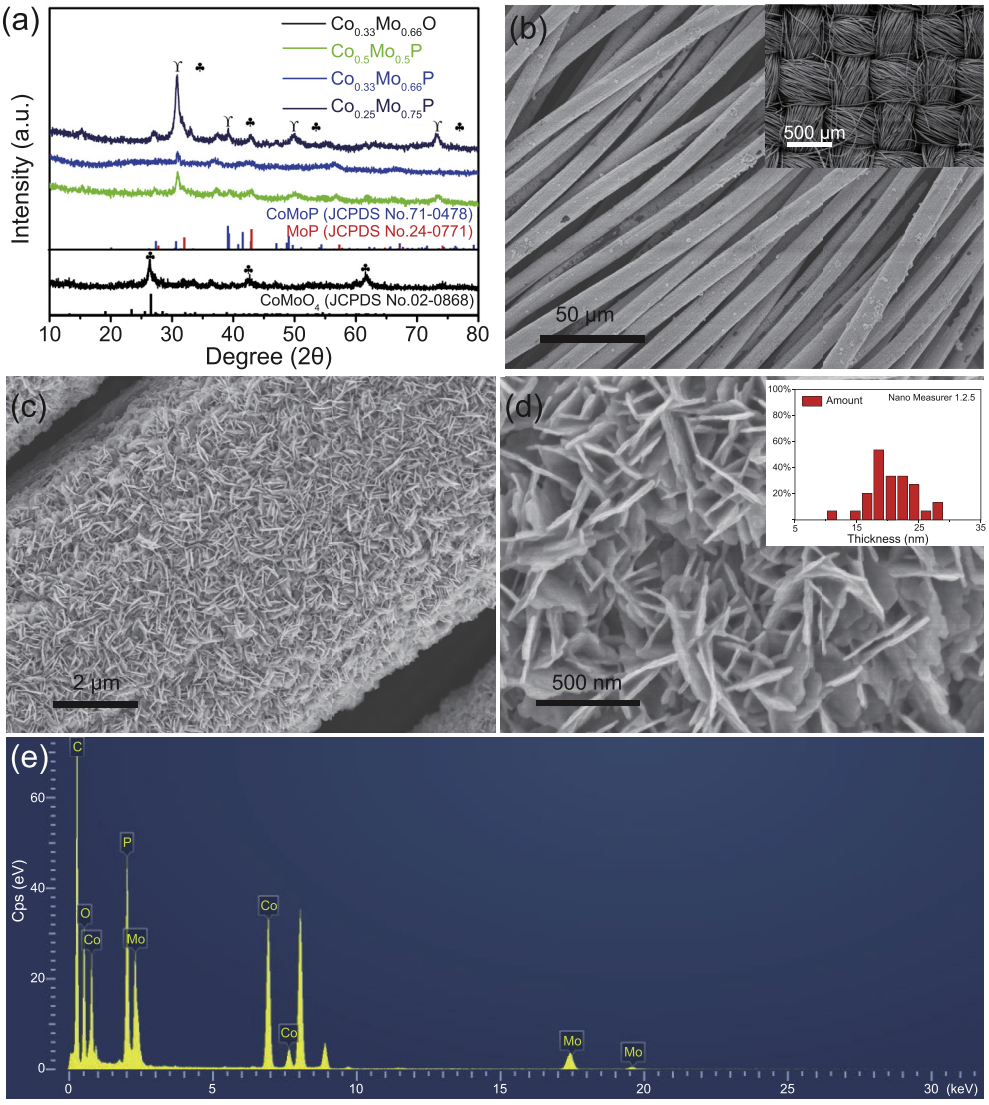

Fig. 2. (a) The XRD patterns of $Co_{0.33}Mo_{0.66}O$ and Co–Mo phosphides in different proportions, (b–d) SEM images of $Co_{0.33}Mo_{0.66}P$ nanosheets grown on carbon fibres. Inset of (b) is a SEM image of the carbon cloth with low magnification; inset of (d) is the thickness distribution of $Co_{0.33}Mo_{0.66}P$ nanosheets. (e) The EDS spectrum of $Co_{0.33}Mo_{0.66}P$.

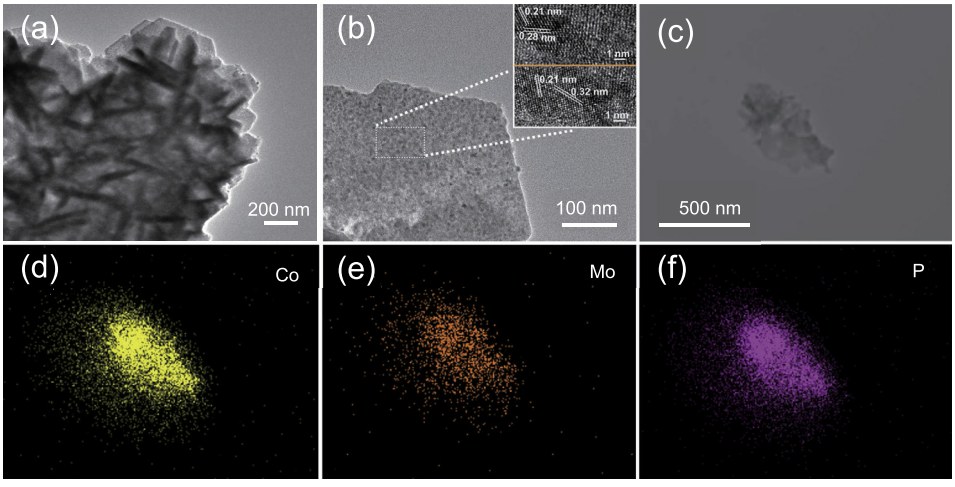

Fig. 3. (a, b) TEM image of $Co_{0.33}Mo_{0.66}P$ nanosheets with different magnification, inset of (b) are the HRTEM images from the nanosheet. (c–f) Elemental mapping images of $Co_{0.33}Mo_{0.66}P$ nanosheet, yellow for Co, orange for Mo and purple for P, respectively.

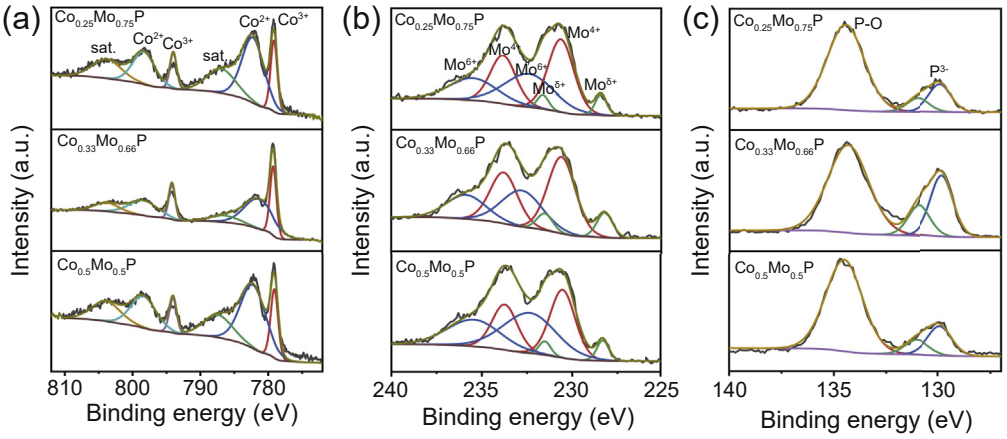

Fig. 4. The XPS spectra of (a) Co 2p, (b) Mo 3d and (c) P 2p of $Co_{0.25}Mo_{0.75}P$, $Co_{0.33}Mo_{0.66}P$ and $Co_{0.50}Mo_{0.50}P$, respectively.

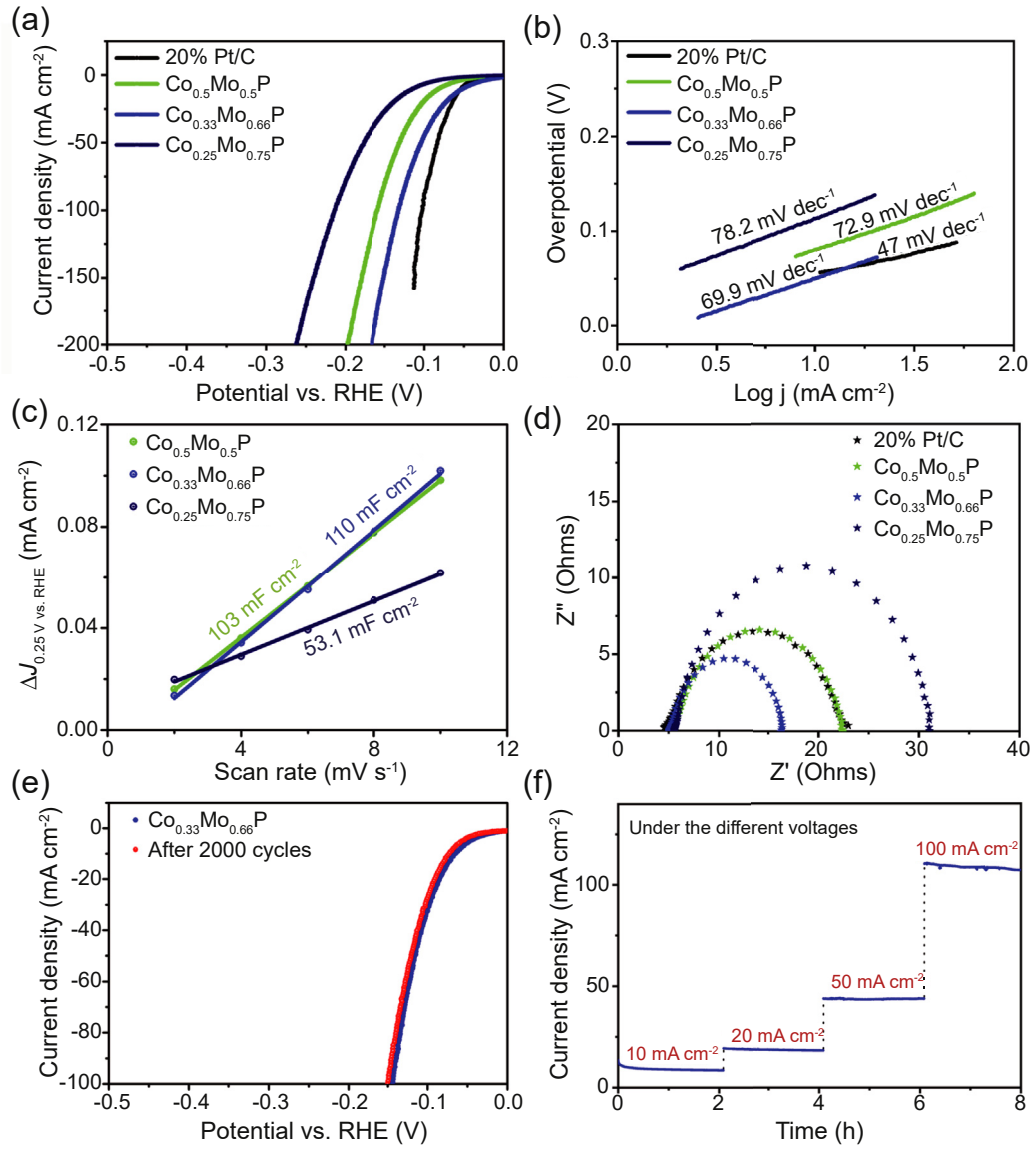

Fig. 5. (a) Polarization curves and (b) Tafel plots of 20% Pt/C, $Co_{0.5}Mo_{0.5}P$, $Co_{0.33}Mo_{0.66}P$ and $Co_{0.25}Mo_{0.75}P$; (c) The capacitive current as a function of the sweep rate for $Co_{0.5}Mo_{0.5}P$, $Co_{0.33}Mo_{0.66}P$ and $Co_{0.25}Mo_{0.75}P$; (d) Nyquist plots of 20% Pt/C, $Co_{0.5}Mo_{0.5}P$, $Co_{0.33}Mo_{0.66}P$ and $Co_{0.25}Mo_{0.75}P$ electrodes; (e) Polarization curves of $Co_{0.33}Mo_{0.66}P$ before and after 2000 cycles; (f) Chronoamperometric curve obtained with the $Co_{0.33}Mo_{0.66}P$ under different voltages.

134.5 eV was assigned to P^{5+} species which could be originated from the surface oxidation of P [26,27]. According to a previous report, a metal complex HER catalyst incorporates protons by the pendant acid-base groups positioned close to the metal center where hydrogen evolution occurs [28].

The HER electrocatalytic performance of $Co_{0.5}Mo_{0.5}P$, $Co_{0.33}Mo_{0.66}P$ and $Co_{0.25}Mo_{0.75}P$ are examined in 1 M KOH and a 20% Pt/C electrode is investigated for comparison. The relevant polarization curves are displayed in Fig. 5a, the overpotential of 67.3 mV is obtained at 10 mA cm^{-2} for $Co_{0.33}Mo_{0.66}P$, which is close to the sample of 20% Pt/C (53 mV). While the overpotential for $Co_{0.5}Mo_{0.5}P$ and $Co_{0.25}Mo_{0.75}P$ are 96 mV and 113 mV, respectively. To acquire the kinetic information of the 20% Pt/C, $Co_{0.5}Mo_{0.5}P$, $Co_{0.33}Mo_{0.66}P$ and $Co_{0.25}Mo_{0.75}P$ electrodes, Fig. 5b displays the corresponding Tafel plots. The $Co_{0.33}Mo_{0.66}P$ exhibits a Tafel slope of 69.9 mV dec^{-1} that is smaller than those of $Co_{0.5}Mo_{0.5}P$ (72.9 mV dec^{-1}) and $Co_{0.25}Mo_{0.75}P$ (78.2 mV dec^{-1}), which indicates the Volmer step could also be the rate-determining step, in addition to the Heyrovsky step Table S1 [29]. Also, this value is comparable to many reported literatures with excellent HER properties Table S2. For further understanding the outstanding catalytic property of the $Co_{0.33}Mo_{0.66}P$, the electrochemical surface area (ECSA) is calculated by CV tests with different scan rates (Fig. S5). The double-layer capacitances (C_{dl}) of $Co_{0.5}Mo_{0.5}P$, $Co_{0.33}Mo_{0.66}P$ and $Co_{0.25}Mo_{0.75}P$ are measured. The C_{dl} is relevant to the ECSA of the catalysts measured with the CV tests from 2 to 10 mV s^{-1}, the $Co_{0.33}Mo_{0.66}P$ shows a larger C_{dl} of 110 mF cm^{-2} than the $Co_{0.5}Mo_{0.5}P$ (103 mF cm^{-2}) and $Co_{0.25}Mo_{0.75}P$ (53.1 mF cm^{-2}), Fig. 5c. The Nyquist plots of the $Co_{0.33}Mo_{0.66}P$ showed a small circle within the low-frequency area, which indicated the faster mass/charge rates (Fig. 5d). Furthermore, a stability test was performed on $Co_{0.33}Mo_{0.66}P$, which is shown in Fig. 5e. The results of the stability test show negligible changes, which proves the excellent stability of the catalyst. Fig. 5f shows multi-step chronoamperometric tests of $Co_{0.33}Mo_{0.66}P$ with the incremental voltage in 1 M KOH solution. During the test, electric currents would be switched every 2 h to test the stability of the electrodes. The current densities of 10, 20, 50 and 100 mA cm^{-2} correspond to the applied voltages (vs. RHE) of 68, 81, 102 and 143 mV. The CA curves further proved the catalysts showed great stability under different working conditions. The OER performance of the catalysts was further investigated. Fig. S6a shows the $Co_{0.33}Mo_{0.66}P$ exhibits the best OER performance and can perform even better than commercial RuO_2 under large current densities. Fig. S6b showed the Tafel plots of $Co_{0.33}Mo_{0.66}P$ is the best (55.2 mV dec^{-1}) among the tested catalysts, which proved the remarkable kinetics of the electrode. Fig. S6d showed the CA curve of $Co_{0.33}Mo_{0.66}P$ at 20 mA cm^{-2}, which indicated the stability of the $Co_{0.33}Mo_{0.66}P$ catalyst is great, even as electrocatalysts for the OER.

Fig. 6a shows the HER stability test of catalysts under 10 mA cm^{-2} for 20 h. The tests show $Co_{0.33}Mo_{0.66}P$ exhibited the best stability with the lowest overpotential. According to Fig. 6b–d, by comparing the change of XPS binding energy

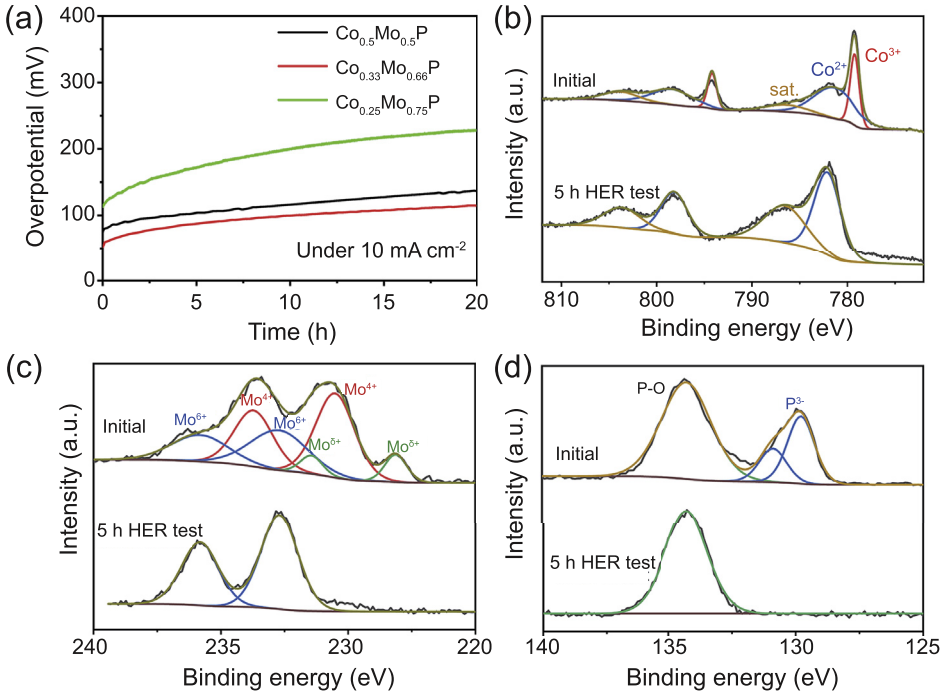

Fig. 6. (a) Polarization curves of Co–Mo phosphides electrodes tested for 20 h at 10 mA cm^{-2}. (b–d) XPS spectra of Co, Mo and P elements before and after 5 h test of $Co_{0.33}Mo_{0.66}P$.

before and after (Fig. S7) the reaction, we can see that the peaks of Co^{3+} in Fig. 6b all disappear, while the peak area of Co^{2+} has no obvious change before and after the HER reaction. It is reasonable that the Co^{3+} species are reduced to Co^{2+} during the HER reaction. It was also observed that there was a change of binding energy of Mo before and after the reaction. The original Mo^{6+} valence still exists, while the peaks of Mo^{4+} and $Mo^{\delta+}$ disappear after the reaction [25]. To further prove the change of the binding energy of P 2p of the materials tested for 5 h, the two peaks of the original metal phosphides disappeared. The P–O peak indicates the formation of metal phosphate group on the surface of the catalyst, which indicates the catalyst suffers from a reconstruction process during the catalysis process in 1M KOH solution. The surface of electrodes could transform from Co–Mo-phosphide to CoMo-phosphate species during HER process in alkaline medium [30].

4. Conclusions

To summarize, a simple approach to obtain Co–Mo phosphides supported on carbon cloth *via* a hydrothermal-annealing process has been developed. Abundant active species were obtained owing to the tuning of the Co and Mo contents with phosphide structures. Superior electrocatalyst performance is obtained. The optimized electrode shows a small overpotential of 67.3 mV with a current density of 10 mA cm^{-2} and a Tafel slope of 69.9 mV dec^{-1}. The electrode also shows an excellent OER performance which indicates this could be a bifunctional catalyst as well. The LSV curves remain effectively unchanged after 2000 CV cycles, demonstrating great stability. This work provides a cost-efficient catalytic hydrogen production material with excellent performance and stability and demonstrates a useful strategy by changing transition metal and phosphorus interactions to optimize the catalytic properties.

Conflict of interest

The authors declare that they have no known competing financial interests or personal relationships that could have appeared to influence the work reported in this paper.

Acknowledgments

The work has been funded by the NSFC (51602193), Shanghai “Chen Guang” Project (16CG63), the Fundamental Research Funds for the Central Universities (WD1817002), the STFC Batteries Network (ST/R006873/1), GH, PRS and DJLB acknowledge funding from the EPSRC (EP/R023581/1, EP/P009050/1).

Appendix A. Supplementary data

Supplementary data related to this article can be found at https://doi.org/10.1016/j.gee.2020.07.009.

References

[1] Z.W. Seh, J. Kibsgaard, C.F. Dickens, I. Chorkendorff, J.K. Nørskov, T.F. Jaramillo, Science 355 (2017) eaad4998.
[2] J. Zhang, Q. Zhang, X. Feng, Adv. Mater. 31 (2019) 1808167.
[3] F. Yu, L. Yu, I.K. Mishra, Y. Yu, Z.F. Ren, H.Q. Zhou, Mater. Today Phys. 7 (2018) 121–138.
[4] Y. Li, X. Tan, S. Chen, X. Bo, H. Ren, S.C. Smith, C. Zhao, Angew. Chem. Int. Ed. 58 (2019) 461–466.
[5] L. Cao, Q. Luo, W. Liu, Y. Lin, X. Liu, Y. Cao, W. Zhang, Y. Wu, J. Yang, T. Yao, S. Wei, Nat. Catal. 2 (2019) 134–141.
[6] M. Cabán-Acevedo, M.L. Stone, J.R. Schmidt, J.G. Thomas, Q. Ding, H. Chang, M. Tsai, J. He, S. Jin, Nat. Mater. 14 (2015) 1245–1251.
[7] F. Haque, A. Zavabeti, B.Y. Zhang, R.S. Datta, Y. Yin, Z. Yi, Y. Wang, N. Mahmood, N. Pillai, N. Syed, H. Khan, A. Jannat, N. Wang, N. Medhekar, K. Kalantar-zadeh, J.Z. Ou, J. Mater. Chem. 7 (2019) 257–268.
[8] M.H. Suliman, A. Adam, M.N. Siddiqui, Z.H. Yamani, M. Qamar, Carbon 144 (2019) 764–771.
[9] T. Ling, T. Zhang, B. Ge, L. Han, L. Zheng, F. Lin, Z. Xu, W.B. Hu, X.W. Du, K. Davey, S.Z. Qiao, Adv. Mater. 31 (2019) 1807771.
[10] L. Yu, L. Wu, B. McElhenny, S. Song, D. Luo, F. Zhang, Y. Yu, S. Chen, Z. Ren, Energy Environ. Sci. 13 (2020) 3439–3446.
[11] X. Dong, H. Yan, Y. Jiao, D. Guo, A. Wu, G. Yang, X. Shi, C. Tian, H. Fu, J. Mater. Chem. 7 (2019) 15823–15830.
[12] S. Xie, B. Sun, H. Sun, K. Zhan, B. Zhao, Y. Yan, B.Y. Xia, Int. J. Hydrogen Energy 44 (2019) 15009–15016.
[13] J. Sun, M. Ren, L. Yu, Z. Yang, L. Xie, F. Tian, Y. Yu, Z. Ren, S. Chen, H. Zhou, Small 15 (2019) 1804272.
[14] Y. Peng, S. Chen, Green Energy Environ. 3 (2018) 335–351.
[15] Y. Jing, H. Liu, R. Yan, J. Chen, H. Dai, C. Liu, X.D. Zhang, ACS Appl. Nano Mater. 2 (2019) 5922–5930.
[16] W. Xiao, L. Zhang, D. Bukhvalov, Z. Chen, Z. Zou, L. Shang, X. Yang, D. Yan, F. Han, T. Zhang, Nano Energy 70 (2020) 104445.
[17] Z.Y. Yu, C.C. Lang, M.R. Gao, Y. Chen, Q.Q. Fu, Y. Duan, S.H. Yu, Energy Environ. Sci. 11 (2018) 1890–1897.
[18] Z. Fang, L. Peng, Y. Qian, X. Zhang, Y. Xie, J.J. Cha, G. Yu, J. Am. Chem. Soc. 140 (2018) 5241–5247.
[19] H.A. Bandal, A.R. Jadhav, A.H. Tamboli, H. Kim, Electrochim. Acta 249 (2017) 253–262.
[20] D. Jiang, Y. Xu, R. Yang, D. Li, S. Meng, M. Chen, ACS Sustain. Chem. Eng. 7 (2019) 9309–9317.
[21] Z. Dai, H. Geng, J. Wang, Y. Luo, B. Li, Y. Zong, J. Yang, Y. Guo, Y. Zheng, X. Wang, Q. Yan, ACS Nano 11 (2017) 11031–11040.
[22] S. Zhao, J. Berry-Gair, W. Li, G. Guan, M. Yang, J. Li, F. Lai, F. Corà, K. Holt, D.J.L. Brett, G. He, I.P. Parkin, Adv. Sci. 7 (2020) 1903674.
[23] M.Q. Yu, L.X. Jiang, H.G. Yang, Chem. Commun. 51 (2015) 14361–14364.
[24] Y. Lin, M. Liu, Y. Pan, J. Zhang, J. Mater. Sci. 52 (2017) 10406–10417.
[25] H. Wu, K. Lian, ECS Trans. 58 (2014) 67–75.
[26] H. Liu, D. Liu, M. Gu, Z. Zhao, D. Chen, P. Cui, L. Xu, J. Yang, Mater. Today Energy 14 (2019) 100336.
[27] H. Zhang, H. Jiang, Y. Hu, H. Jiang, C. Li, Green Energy Environ. 2 (2017) 112–118.
[28] B.E. Barton, T.B. Rauchfuss, J. Am. Chem. Soc. 132 (2010) 14877–14885.
[29] R. Xu, L. Kang, J. Knossalla, J. Mielby, Q. Wang, B. Wang, J. Feng, G. He, Y. Qin, J. Xie, A.C. Swertz, Q. He, S. Kegnæs, D.J.L. Brett, F. Schüth, F.R. Wang, ACS Nano 13 (2019) 2463–2472.
[30] Z. Wu, L. Huang, H. Liu, H. Wang, ACS Catal. 9 (2019) 2956–2961.